HUBBLE SPACE TELESCOPE NEAR-IR TRANSMISSION SPECTROSCOPY OF THE SUPER-EARTH HD 97658B

Heather A. Knutson[1,2], Diana Dragomir[3,4], Laura Kreidberg[5], Eliza M.-R. Kempton[6], P. R. McCullough[7], Jonathan J. Fortney[8], Jacob L. Bean[5], Michael Gillon[9], Derek Homeier[10], Andrew W. Howard[11]

Draft version March 20, 2014

ABSTRACT

Recent results from the *Kepler* mission indicate that super-Earths (planets with masses between $1-10$ times that of the Earth) are the most common kind of planet around nearby Sun-like stars. These planets have no direct solar system analogue, and are currently one of the least well-understood classes of extrasolar planets. Many super-Earths have average densities that are consistent with a broad range of bulk compositions, including both water-dominated worlds and rocky planets covered by a thick hydrogen and helium atmosphere. Measurements of the transmission spectra of these planets offer the opportunity to resolve this degeneracy by directly constraining the scale heights and corresponding mean molecular weights of their atmospheres. We present *Hubble Space Telescope* near-infrared spectroscopy of two transits of the newly discovered transiting super-Earth HD 97658b. We use the Wide Field Camera 3's scanning mode to measure the wavelength-dependent transit depth in thirty individual bandpasses. Our averaged differential transmission spectrum has a median 1σ uncertainty of 19 ppm in individual bins, making this the most precise observation of an exoplanetary transmission spectrum obtained with WFC3 to date. Our data are inconsistent with a cloud-free solar metallicity atmosphere at the 17σ level. They are a good match for flat models corresponding to either a metal-rich atmosphere or a solar metallicity atmosphere with a cloud or haze layer located at pressures of a mbar or higher.

Subject headings: binaries: eclipsing — planetary systems — techniques: spectroscopy

1. INTRODUCTION

The *Kepler* mission has resulted in the discovery of more than three thousand transiting planets and planet candidates (Batalha et al. 2013; Burke et al. 2014) to date, with a majority of the sample consisting of sub-Neptune-sized planets. Analyses of this set of Kepler planet candidates indicate that planets with radii intermediate between that of Neptune and the Earth appear to be the most common kind of extrasolar planet orbiting nearby FGK stars, with a peak at radii between $2-3\times$ that of the Earth (Howard et al. 2012; Fressin et al. 2013; Petigura et al. 2013). Planets in this size range are typically referred to as "super-Earths", although they could potentially form with a broad range of compositions including primarily rocky with a thin atmosphere (true "super-Earths"), a rocky or icy core surrounded by a thick hydrogen atmosphere ("mini-Neptunes"), or water-dominated with a thick steam atmosphere ("water worlds"). Many of these super-Earths are found in close-in, tightly packed multiple planet systems (e.g., Lissauer et al. 2011; Fabrycky et al. 2012; Steffen et al. 2013), and there is an ongoing debate as to whether these systems formed in place or migrated in from more distant orbits (Hansen & Murray 2012; Chiang & Laughlin 2013; Raymond & Cossou 2014).

Detailed studies of super-Earth compositions offer important clues on their origins: presumably water-rich planets must have formed beyond the ice line, while in-situ formation models predict primarily rocky compositions with relatively water-poor hydrogen-dominated atmospheres (e.g., Raymond et al. 2008). By combining radius measurements from *Kepler* with mass estimates obtained using either the radial velocity or transit timing techniques, it is possible to constrain the average densities and corresponding bulk compositions of the super-Earths in the Kepler sample (e.g., Lithwick et al. 2012; Hadden & Lithwick 2013; Weiss & Marcy 2014; Marcy et al. 2014). These observations indicate that the super-Earths in the Kepler sample display a broad range of average densities, with a transition towards denser, primarily rocky compositions below $1.5-2$ Earth radii (Weiss & Marcy 2014; Marcy et al. 2014). For the larger, lower-density super-Earths in the Kepler sample it is possible to match their measured densities with a broad range of compositions, including both water-rich and water-poor scenarios, simply by varying the amount of hydrogen in their atmospheres (Seager et al. 2007; Valencia et al. 2007, 2013; Rogers & Seager 2010a; Zeng & Sasselov 2013). Although it can be argued that some compositions are unlikely based on mod-

[1] Division of Geological and Planetary Sciences, California Institute of Technology, Pasadena, CA 91125, USA
[2] hknutson@caltech.edu
[3] Las Cumbres Observatory Global Telescope Network, Goleta, CA 93117, USA
[4] Department of Physics, Broida Hall, UC Santa Barbara, CA, USA
[5] Department of Astronomy and Astrophysics, University of Chicago, Chicago, IL 60637, USA
[6] Department of Physics, Grinnell College, Grinnell, IA 50112 USA
[7] Space Telescope Science Institute, Baltimore, MD 21218, USA
[8] Department of Astronomy and Astrophysics, University of California, Santa Cruz, CA 95064 USA
[9] Institut d'Astrophysique et de Géophysique, Universiteé de Liége, Liége 1, Belgium
[10] Centre de Recherche Astrophysique de Lyon, 69364 Lyon, France
[11] Institute for Astronomy, University of Hawaii at Manoa, Honolulu, HI, USA

els of planet formation and atmospheric mass loss for close-in planets, this still leaves a wide range of plausible models (e.g., Rogers & Seager 2010b; Rogers et al. 2011; Nettelmann et al. 2011; Heng & Kopparla 2012; Lopez et al. 2012; Lopez & Fortney 2013; Fortney et al. 2013).

Measurements of the transmission spectra of super-Earths allow us to directly estimate the mean molecular weight of the planet's atmosphere (e.g., Miller-Ricci et al. 2008; Fortney et al. 2013), which in turn provides improved constraints on its interior composition. Planets with cloud-free, hydrogen dominated atmospheres will have relatively large scale heights and correspondingly strong absorption features during transit, while planets with hydrogen-poor atmospheres will have relatively small scale heights and weak absorption. Unfortunately, the majority of the super-Earths detected by Kepler orbit faint stars ($m_K > 10$), making it difficult to accurately measure their transmission spectra using existing facilities. There are currently three super-Earths known to transit relatively bright stars, including: GJ 1214b ($m_K = 8.8$; Charbonneau et al. 2009), 55 Cancri e ($m_K = 4.0$; Winn et al. 2011; Demory et al. 2011), and HD 97658b ($m_K = 5.7$; Dragomir et al. 2013).

GJ 1214b is currently the only one of these three systems with a well-characterized transmission spectrum, which is flat and featureless across a broad range of wavelengths (e.g., Bean et al. 2010, 2011; Désert et al. 2011; Berta et al. 2012; Kreidberg et al. 2014). Although initial observations were consistent with either a cloud-free, hydrogen-poor atmosphere or a hydrogen-rich atmosphere with a high cloud deck (e.g., Bean et al. 2010), the most recent near-IR observations obtained by Kreidberg et al. (2014) using the Wide Field Camera 3 (WFC3) instrument on the *Hubble Space Telescope (HST)* are precise enough to rule out cloud-free models over a broad range of atmospheric metallicities (also see Benneke & Seager 2013). The presence of a high altitude cloud or haze layer means that for this planet, at least, transmission spectroscopy provides relatively weak constraints on the mean molecular weight of its atmosphere and, by extension, on its interior composition.

In this paper we present *HST* WFC3 near-infrared transmission spectroscopy of the transiting super-Earth HD 97658b. This planet was first detected using the radial velocity technique (Howard et al. 2011), and later found to transit using *MOST* photometry (Dragomir et al. 2013) . It has a mass of 7.9 ± 0.7 $M_\oplus$, a radius of 2.3 ± 0.2 $R_\oplus$, and an average density of 3.4 ± 0.9 g cm^{-1} (Dragomir et al. 2013), making it modestly denser and more massive than GJ 1214b. HD 97658b orbits its K star primary with a period of 9.5 days, and has a predicted zero-albedo temperature between $700 - 1000$ K depending on the efficiency of energy transport to the planet's night side. If this planet has the same atmospheric composition as GJ 1214b, its modestly higher atmospheric temperature might prevent the formation of the cloud layer detected in GJ 1214b's atmosphere (Morley et al. 2013). Our observations are obtained at wavelengths between $1.2 - 1.6$ μm, and are primarily sensitive to the presence or absence of the water absorption band located at 1.4 μm; this feature has now been robustly detected in the atmospheres of several hot Jupiters (e.g.,
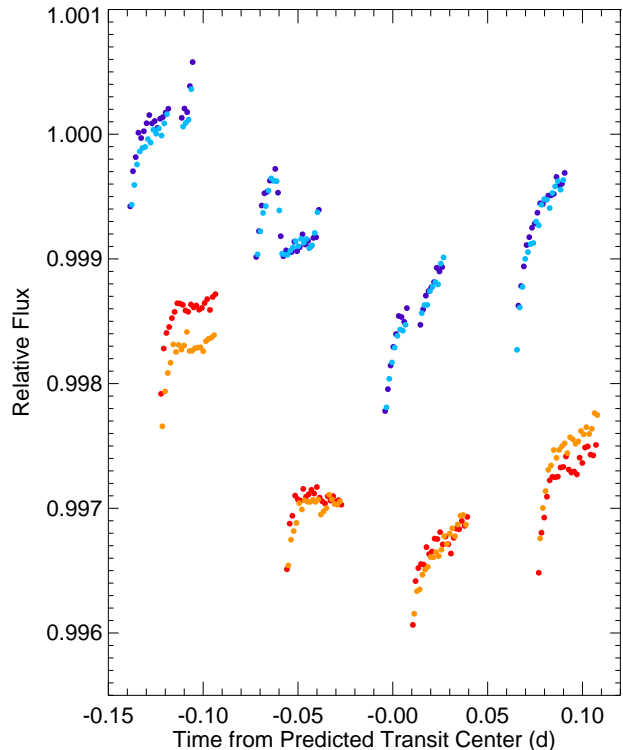

FIG. 1.— Raw white light photometry for the UT 2013 Dec 19 visit (top) and UT 2014 Jan 7 transit (bottom). Different scan directions for the December visit are indicated as light (forward scan) and dark (reverse scan) blue filled circles. Scan directions for the January visit are plotted as yellow (forward scan) and red (reverse scan) filled circles. The two light curves have been offset by a relative flux of 0.0015 for clarity. The first spacecraft orbit has been trimmed from each visit, leaving four orbits per transit. We have also normalized the light curves from each scan direction to one by dividing each by the median flux value; we do this in order to remove a small offset in the measured fluxes from the two scan directions.

Deming et al. 2013; Wakeford et al. 2013; Mandell et al. 2013; McCullough et al. 2014), and is expected to be present in super-Earths as well over a broad range of atmosphere compositions (e.g., Benneke & Seager 2012; Kreidberg et al. 2014; Hu & Seager 2014). We discuss our observations in §2 and the implications for the properties of this planet's atmosphere in §3.

2. OBSERVATIONS

We observed one transit of HD 97658b on UT 2013 Dec 19 and another on UT 2014 Jan 7 (GO 130501, PI Knutson) using the G141 grism on the *HST* WFC3 instrument, which provides low resolution spectroscopy at wavelengths between $1.1 - 1.7$ μm. Each observation consists of five *HST* orbits with a total duration of approximately seven hours per visit; our target was visible for approximately half of each 96 minute *HST* orbit. Scheduling constraints resulted in a slightly shorter first orbit during the January visit, which consisted of 203 spectra instead of the 206 spectra obtained during the December visit. During the January visit we also utilized a series of short exposures at the end of each orbit in order to force a buffer dump, which avoided the mid-orbit gaps in coverage visible in the light curves for the first visit in Fig. 1. We do not include these short ex-

posures in our analysis, as they were taken in imaging rather than spectroscopic mode.

Our spectra were obtained using the 256×256 pixel subarray and SPARS10 mode with four samples, giving a total integration time of 14.97 s in each image. Our target is one of the brightest transiting planet host stars, and we therefore utilized the new scanning mode (e.g., McCullough & MacKenty 2012; Deming et al. 2013; Kreidberg et al. 2014; Knutson et al. 2014) with a scan rate of $1.4'' \text{ s}^{-1}$ in order to achieve a higher observing efficiency while remaining well below saturation. This results in a scanned spectral image that fills most of the subarray image, with a fractional coverage similar to that of the HD 209458 observations from Deming et al. (2013). We also alternated between forward and reverse scan directions in order to further reduce overheads; this approach was previously used by Kreidberg et al. (2014) for GJ 1214b. The resulting spectra have peak counts around 40,000 electrons pixel^{-1}, which is high enough to cause a modestly steep asymptotic ramp in the measured fluxes within individual orbits (see Wilkins et al. 2014, for a discussion of the relationship between the ramp slope and total flux).

We reduced the data using two independent methods, which allow us to test whether or not the transmission spectrum we obtain from our analysis is sensitive to our choice of analysis technique. We discuss each approach separately below.

2.1. Spectral Template Fitting Method

In this approach we utilized the spectral template method first presented in Deming et al. (2013), which we describe in detail in Knutson et al. (2014) and summarize here. We begin with the raw sample up the ramp images from the ima.fits files, which are bias and dark subtracted, and apply our own flat-fielding and wavelength calibrations based on the standard WFC3 pipeline as discussed in Wilkins et al. (2014). We then subtract successive non-destructive readout pairs in order to create a series of difference images, trim the region around the spectral scan in each image, and sum the resulting images to create a composite containing the full scan. The benefit of this approach is that it avoids the need for a separate sky background subtraction step by minimizing the contributions of pixels that are not directly illuminated by the star in a given readout time step (see Deming et al. 2013, for more discussion on this point). We estimate that the sky background for our final composite images is $0.18 - 0.24\%$ of the total flux measured in each wavelength element. Subtracting this flux would reduce our measured transit depths by approximately two ppm, which is much less than our measurement errors at all wavelengths.

Once we have created a stacked image from each set of readouts, we apply a filter to correct for bad pixels and cosmic ray hits as described in Knutson et al. (2014). We then sum the spectrum along the y axis in order to extract a one dimensional spectrum, using an aperture that extends fifteen pixels above and below the edges of the spectrum (200 pixels in total) in order to include the extended wings of the point spread function (see Fig. 2 for a representative example). Because the WFC3 spectra are undersampled (Deming et al. 2013), we convolve each of our one dimensional spectra with a Gaussian function
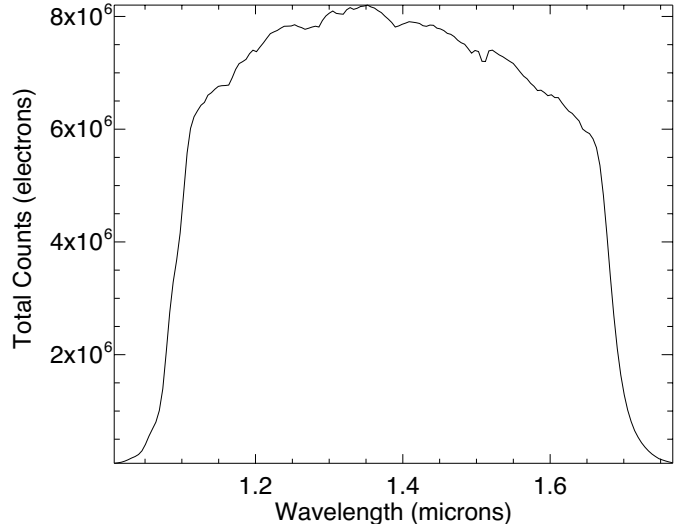

Fig. 2.— A representative spectrum from the UT 2013 Dec 19 visit; this spectrum was created from the two dimensional image by summing in the y (cross-dispersion) direction.

with a width (FWHM) of four pixels in order to mitigate effects related to the shifting position of the spectrum on the detector. Although this modestly degrades the spectral resolution of our data, we later bin our transmission spectrum by an equivalent amount in order to increase the signal to noise ratio. We calculate the MJD mid-exposure time corresponding to each image using the information from the flt.fits image headers, and convert these times to the BJD$_{TDB}$ time standard following the methods of Eastman et al. (2010).

Our next step is to create a spectral template by averaging the ten spectra immediately before and after the transit. We then fit this template spectrum to each individual spectrum in our time series, allowing the relative position and amplitude of the template spectrum to vary as free parameters. We find no difference in our results if we create a separate spectral template for the forward and reverse scan images, and we therefore use the same template for all images. The resulting series of best-fit amplitudes are plotted in Fig. 1, and are identical to the white-light curves obtained by summing the fluxes across all wavelengths. We find that there is a small flux offset between the light curves for the two scan directions, which we remove by dividing each time series by its median flux value. McCullough & MacKenty (2012) suggest that this offset is a consequence of the order in which columns are read out by the detector (the "upstream/down-stream effect"); when the scan moves in the same direction as the readout then the effective integration time will be slightly longer than in the case of a reverse scan. The forward and reverse spectra in our images also occupy slightly different positions on the array, which might also contribute to this offset.

We subtract the best-fit spectral template from each individual spectrum in order to create a differential time series for each individual wavelength element. The benefit to this approach is that it effectively removes all common-mode detector effects from the differential light curve. We find that the scatter in our light curves for individual wavelength elements is within 5% of the photon noise limit in all cases, indicating that there is minimal
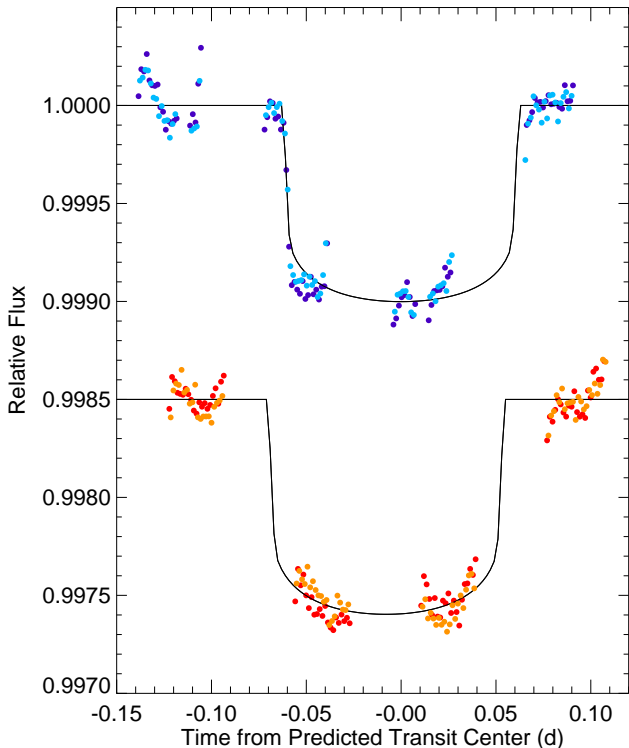
FIG. 3.— Normalized white light photometry with best-fit detector effects removed for the UT 2013 Dec 19 visit (top) and UT 2014 Jan 7 transit (bottom). Different scan directions for the December visit are indicated as light (forward scan) and dark (reverse scan) blue filled circles. Scan directions for the January visit are plotted as yellow (forward scan) and red (reverse scan) filled circles. The first spacecraft orbit has been trimmed from each visit, leaving four orbits per transit, and the two light curves have been offset by a relative flux of 0.0015 for clarity.
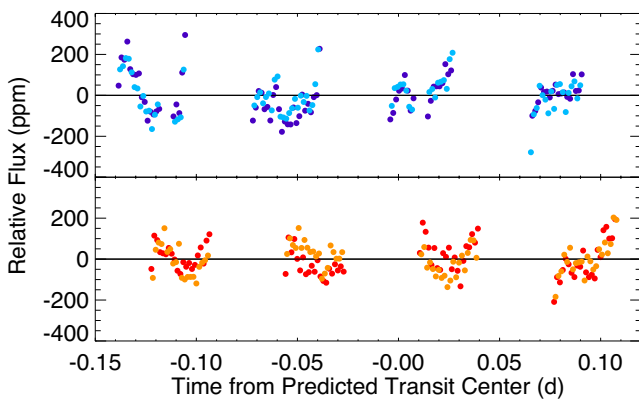

FIG. 4.— White light residuals after the best-fit detector and transit light curves are removed for the UT 2013 Dec 19 visit (top panel) and UT 2014 Jan 7 transit (bottom panel). Different scan directions for the December visit are indicated as light (forward scan) and dark (reverse scan) blue filled circles. Scan directions for the January visit are plotted as yellow (forward scan) and red (reverse scan) filled circles.

color-dependence in the systematic noise sources.

2.1.1. *White Light Transit Fits*

We take the two raw transit light curves plotted in Fig. 1 and fit them each with a transit light curve, a linear function of time, and an exponential ramp in orbital phase:

$$F(t) = c_1(1 + c_2 t + c_3 e^{-p/c_4})F_{transit}(t) \qquad (1)$$

where $c_1 - c_4$ are free parameters in the fit, t is the time from the measured transit center in days and p is the time in days from either the first observation in each spacecraft orbit or the last observation before a mid-orbit buffer dump. We use this definition because we find that the ramp after a mid-orbit buffer dump is usually not as steep as the initial ramp at the start of the orbit, and using this definition provided a good fit to the observed behavior by reducing the amplitude of the mid-orbit ramp model. The latter definition is only used for the December transit observation, which includes two mid-orbit buffer dumps that cause the ramp effect to reset. We calculate the transit light curve $F_{transit}$ following Mandel & Agol (2002) where we fix the orbital inclination i and the ratio of the semi-major axis to the stellar radius $a/R_\star$ equal to their best-fit values from Van Grootel et al. (2014). We allow the planet-star radius ratio $R_p/R_\star$ and center of transit time to vary as free parameters for each individual transit. We find that the behavior of the instrumental systematics is slightly different for the white light curves calculated from the forward and reverse scan directions (see Fig. 1). We therefore allow the linear function of time and exponential ramp functions to vary independently for each scan direction, while keeping the same $R_p/R_\star$ and center of transit time.

We calculate our initial predicted transit times using the ephemeris from Van Grootel et al. (2014), and then derive an updated estimate for the orbital period and center of transit time based on our new observations. We then repeat our transit fits using this updated orbital period. We calculate four-parameter nonlinear limb-darkening parameters (Claret 2000) for our transit light curves, with the relative intensity at each position given as:

$$\frac{I(\mu)}{I(1)} = 1 - \sum_{k=1}^{4} a_k(1 - \mu^{k/2}) \qquad (2)$$

where $I(1)$ is the specific intensity at the center of the stellar disk, a_k is the kth limb-darkening coefficient, and $\mu = cos(\theta)$ where θ is the angle between the the line of sight and the location of the emerging flux. We calculate our limb-darkening coefficients using a PHOENIX stellar atmosphere model(Allard et al. 2012), where we take the flux-weighted average of the stellar intensity profile across the band and then fit for the limb-darkening coefficients. We use the best-fit stellar parameters from Van Grootel et al. (2014), who find an effective temperature of 5170 ± 50 K, a surface gravity of 4.58 ± 0.05, and a metallicity of -0.23 ± 0.03. These values are also consistent with a recent analysis by Mortier et al. (2013), although this study prefers a lower metallicity of -0.35 ± 0.02 and does not take into account the constraints on the stellar density from the transit light curve. We also tried models with effective temperatures ranging between $5120 - 5220$ K and a metallicity of -0.35, but found that these had a negligible effect on our resulting transmission spectrum. The inclusion of limb-darkening in our fits creates a small offset in the average transit

<div style="text-align:center">

TABLE 1
WHITE LIGHT TRANSIT PARAMETERS

</div>

Parameter	Value
Global Values	
$i(°)$[a]	89.14
$a/R_\star$[a]	23.32
P (days)[b]	9.489420 ± 0.000047
T_0 (BJD$_{TDB}$)[b]	$2456665.46678 \pm 0.00032$
UT 2013 Dec 19 Transit	
$R_p/R_\star$	0.03000 ± 0.00081
T_c (BJD$_{TDB}$)	$2456646.48821 \pm 0.00036$[c]
UT 2014 Jan 7 Transit	
$R_p/R_\star$	0.03140 ± 0.00079
T_c (BJD$_{TDB}$)	2456665.4588 ± 0.0072[c]

[a] These values were taken from Van Grootel et al. (2014) and fixed in our fits. We also tried fits where these parameters were allowed to vary freely over $\pm 1\sigma$ and found this had a negligible effect on the errors for the radius ratios and transit times.
[b] We calculate our updated ephemeris using the published transit times from Dragomir et al. (2013) and Van Grootel et al. (2014) and our two new transit measurements. T_0 is the zero epoch transit center time from our best-fit ephemeris, and T_c is the measured transit center time from a given observation.
[c] The errors on our fitted transit times increase to approximately five minutes when we allow $a/R_\star$ and i to vary as free parameters in our fits.

depth as compared to fits without limb-darkening, and modestly alters the slope of the resulting transmission spectrum across the bandpass.
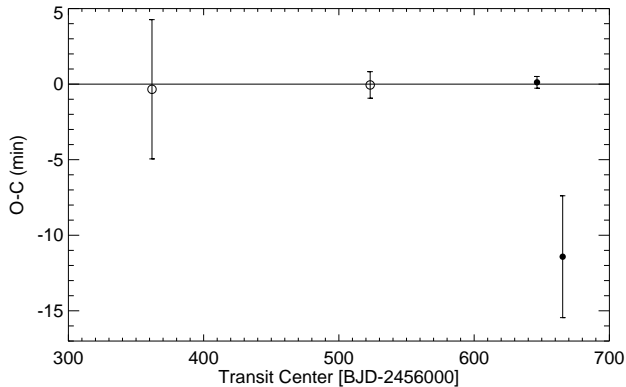

FIG. 5.— Observed minus calculated transit times using our updated ephemeris. Previously published *MOST* (Dragomir et al. 2013) and *Spitzer* transit times (Van Grootel et al. 2014) are shown as open circles, with our new *HST* observations are shown as filled circles. The second *HST* transit has a larger uncertainty on the transit time because it does not include any points during ingress or egress, which provide the strongest constraints on the measured center of transit time.

We estimate the uncertainties in our fitted white light parameters using both a residual permutation ("prayer bead") method and the covariance matrix from our Levenberg-Marquart minimization, where we have set the uncertainties on individual points in our time series equal to the standard deviation of the residuals from our best-fit solution. Although we do not carry out a full Markov Chain Monte Carlo (MCMC) analy-

<div style="text-align:center">

TABLE 2
BINNED FOUR PARAMETER NONLINEAR
LIMB-DARKENING COEFFICIENTS[a]

</div>

Wavelength[b]	c_1	c_2	c_3	c_4
1.133	0.6247	-0.4071	0.6890	-0.3099
1.152	0.6489	-0.4619	0.7545	-0.3395
1.171	0.6710	-0.5019	0.7856	-0.3530
1.190	0.6925	-0.5644	0.8445	-0.3743
1.208	0.7275	-0.6442	0.9250	-0.4065
1.227	0.7631	-0.7246	1.0242	-0.4507
1.246	0.8020	-0.8191	1.1222	-0.4894
1.265	0.8576	-0.9453	1.2552	-0.5437
1.284	0.4703	0.1247	0.0695	-0.0947
1.303	0.5182	-0.01457	0.2336	-0.1563
1.321	0.5640	-0.1255	0.3410	-0.1967
1.340	0.6366	-0.2849	0.5109	-0.2661
1.359	0.7125	-0.4597	0.6892	-0.3356
1.378	0.8012	-0.6639	0.8937	-0.4138
1.397	0.8842	-0.8546	1.0907	-0.4911
1.416	0.8901	-0.8644	1.1018	-0.4975
1.434	1.0237	-1.1944	1.4386	-0.6244
1.453	1.1298	-1.4436	1.6910	-0.7202
1.472	1.2482	-1.7152	1.9657	-0.8248
1.491	0.4779	0.4024	-0.4201	0.1113
1.510	0.5016	0.3492	-0.3886	0.1055
1.529	0.5557	0.3381	-0.4372	0.1307
1.547	0.6129	0.2520	-0.3962	0.1249
1.566	0.6479	0.1523	-0.3120	0.1000
1.585	0.6325	0.1655	-0.3350	0.1121
1.604	0.7095	0.0517	-0.2727	0.0993
1.623	0.7208	0.0239	-0.2472	0.0905
1.642	0.7129	0.0421	-0.2933	0.1144

[a] The spectra extracted from the UT 2013 Dec 19 and UT 2014 Jan 7 visits have slightly different wavelength solutions, and we therefore created custom limb darkening coefficients for each visit. A full table of both the binned and unbinned coefficients for both visits is available upon request.
[b] These binned coefficients are only used in the white light residual fitting analysis. In the spectral template fitting analysis we fit the light curves for individual wavelength elements and use limb-darkening coefficients calculated appropriately for this resolution (4x higher than shown here).

sis, we demonstrated in Knutson et al. (2014) that this approach produces errors that are equivalent to those from the covariance matrix for WFC3 transit observations. We find that for our observations of HD 97658b the residual permutation technique results in uncertainties that are $2-3$ times larger than the corresponding values from the covariance matrix. This is expected, as the noise in our white light curves is dominated by time-correlated instrument effects, while the MCMC and covariance methods implicitly assume random Gaussian-distributed noise (Carter & Winn 2009). We give our best-fit transit parameters in Table 1, and plot the normalized transit light curves after dividing out our best fit for detector effects in Fig. 3. The white light curve residuals from UT 2013 Dec 19 and UT 2014 Jan 7 have a rms of [96,90] ppm and [79,74] ppm, respectively, where we calculate this number separately for data from the forward and reverse scan directions. We show the residuals from these fits in Fig. 4, and the offset between the observed and calculated transit times from our updated orbital ephemeris in Fig. 5. The second transit does not have any measurements during ingress or egress, and therefore has a correspondingly large uncertainty on the measured center of transit time.

TABLE 3
WAVELENGTH DEPENDENT TRANSIT DEPTHS FROM
TEMPLATE FITTING METHOD

Wavelength μm	Depth ppm	Meas. Error[a] ppm	Syst. Error[a] ppm
1.132	926	22	1
1.151	911	28	1
1.170	930	18	1
1.188	927	16	1
1.207	924	17	1
1.226	911	16	1
1.245	906	17	1
1.264	949	15	1
1.283	965	16	1
1.301	967	17	1
1.320	960	18	1
1.339	947	21	1
1.358	945	22	1
1.377	932	25	1
1.396	923	17	1
1.415	926	27	1
1.433	984	23	1
1.452	948	21	1
1.471	966	19	1
1.490	949	19	1
1.509	969	23	1
1.528	975	18	1
1.546	952	17	1
1.565	943	24	1
1.584	970	20	1
1.603	981	19	1
1.622	975	19	1
1.641	965	25	1

[a] Measurement errors reflect the uncertainty in the data, while the systematic errors account for the additional uncertainty in the limb-darkening models from the stellar effective temperature.

2.1.2. *Differential Transit Fits*

We estimate the planet's wavelength-dependent transit depth by fitting the differential time series for each individual wavelength element. In this case we fit the differential time series for all five orbits rather than the four used in the white light fits, as we find that the differential light curves do not show any detectible systematic trends during the first orbit. The light curves for the forward and reverse scans are offset by a constant flux value, so we divide each light curve by its median value before carrying out our fit. We fit each light curve with a linear function of time and a transit function calculated as the difference between the transit light curve in that band and the white-light transit curve. We also tried fits where we allowed an independent linear function of time for each scan direction, but found that this gave a transmission spectrum that was indistinguishable from the case where we assumed the same linear function for both scan directions. We use the best-fit transit time from the white light fits, and fit for the planet-star radius ratio $R_p/R_\star$ corresponding to each wavelength element. The best-fit transit depths reported in Table 3 are simply the square of these values.

We calculate the appropriate four-parameter nonlinear limb-darkening coefficients for each wavelength element using the same PHOENIX model used for the white-light fits (see Table 2), where we convolve the model spectrum at each position on the star with the same Gaussian function used on our data before fitting for the limb-darkening coefficients. We find that varying the stellar
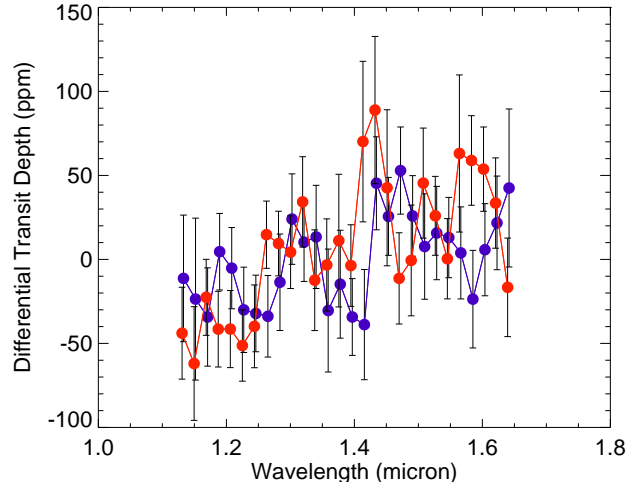

FIG. 6.— Wavelength-dependent relative transit depths measured for the UT 2013 Dec 19 (blue filled circles) and UT 2014 Jan 7 (red filled circles) visits. The white-light transit depths have been subtracted from each visit.

effective temperature by ± 50 K has a minimal effect on our resulting transmission spectrum, which we quantify and include as a separate systematic error term in Table 3.

We estimate uncertainties in the best-fit planet star radius ratios for each wavelength element using both a residual permutation method and the covariance matrix from our Levenberg-Marquart minimization, where we have set the uncertainties on individual points equal to the standard deviation of the out of transit time series. We take the larger of these two errors at each wavelength; our resulting uncertainties are typically 5% larger than the predicted photon noise limited values. Next we bin the resulting wavelength-dependent radius values by a factor of four to create the transmission spectrum shown in Fig. 6, where we average the estimated radii and corresponding errors in each of the twenty eight bins. We then take the error-weighted average of the two individual transmission spectra to create the combined spectrum shown in Fig. 7 and in Table 3.

As an additional consistency check, we also carried out a version of our analysis in which we allowed the light curves derived from the forward and reverse scans to have different planet-star radius ratios. We found that we obtained consistent radius estimates from both scan directions, indicating that the different behaviors visible in the white-light curves are effectively removed in the differential time series by our template fitting technique.

2.2. *White Light Residual Fitting Method*

We also obtained an independent estimate of the transmission spectrum following the approach of Kreidberg et al. (2014). In this analysis we treated each up-the-ramp sample in the ima.fits images as an independent subexposure. For each subexposure, we interpolated all rows to a common wavelength scale to account for the changing dispersion solution with spatial position on the detector. We estimated the background by making conservative masks around the stellar spectra and taking the median of the unmasked pixels. We subtracted the background and optimally extracted the

TABLE 4
WAVELENGTH DEPENDENT TRANSIT DEPTHS FROM
WHITE LIGHT RESIDUAL METHOD

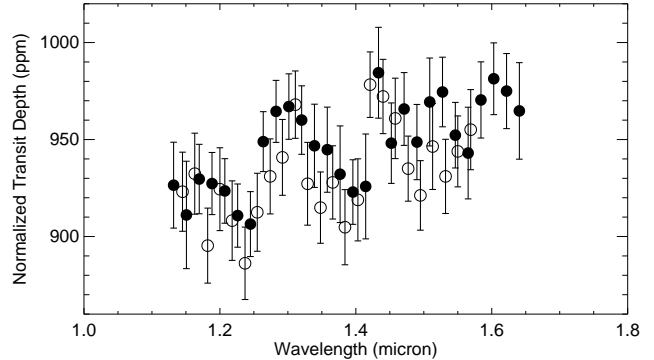| Wavelength μm	Depth ppm	Meas. Error ppm	Reduced χ^2
1.145	923	20	1.31
1.163	932	21	0.99
1.182	895	19	1.04
1.200	924	21	0.78
1.218	908	21	0.96
1.237	886	19	0.83
1.255	913	20	0.76
1.274	931	19	1.02
1.292	941	20	1.02
1.311	968	17	1.58
1.329	927	21	0.86
1.348	915	18	0.82
1.366	928	19	1.05
1.384	905	19	1.04
1.403	919	21	0.93
1.421	978	17	0.86
1.440	972	19	1.03
1.458	961	21	1.38
1.477	935	17	1.26
1.495	921	18	0.98
1.513	946	22	2.18
1.532	931	19	1.26
1.550	944	18	1.19
1.569	955	21	1.39

FIG. 7.— Wavelength-dependent transit depths averaged over the two visits, where the depths are defined as the square of the planet-star radius ratio $R_p/R_\star$ in each band. Depths derived using the spectral template fitting technique (Deming et al. 2013; Knutson et al. 2014) are shown as filled circles, and depths from the white light residual fitting technique (Kreidberg et al. 2014) are shown as open circles. No offset has been applied to either data set, demonstrating that the average transit depths are also in good agreement.

spectra. To combine the data from individual subexposures, we summed the spectra by column. The final step in the reduction process is to correct for drift of the spectra in the dispersion direction over the course of a visit. We used the first exposure from the first visit as a template and shifted all subsequent spectra to the template wavelength scale. The spectra shifted by a total of 0.3 pixels over the five orbits contained in our observations, which is larger than the approximately 0.01 pixel drift observed in previous scanning mode observations of GJ 1214b (Kreidberg et al. 2014). This increased drift may be related to the longer scan length and faster scan rate utilized for these observations as compared to GJ 1214b.

We binned the spectra in four-pixel-wide channels, yielding 24 spectrophotometric light curves between 1.15 and 1.57 μm. The light curves show orbit-long ramp-like systematics that are characteristic of WFC3 data. We correct for these systematics using the divide-white technique, which assumes that the observed effects have the same shape across all wavelengths. We fit each spectroscopic light curve with a transit model multiplied by a scaled vector of systematics from the best-fit white light curve. The fit to each channel has five free parameters: one transit depth and four scaling factors for the systematics (one for each visit and scan direction). As before, we calculate the four-parameter nonlinear limb-darkening coefficients using a PHOENIX stellar atmosphere model and integrating across each photometric bandpass. The uncertainty on the transit depths corresponds to 1σ confidence intervals from an MCMC fit, where we set the uncertainties on individual points equal to the sum of the the photon noise and read noise in quadrature.

These errors are nearly identical to the rms to the best fit for each spectroscopic channel. We list the best-fit values and corresponding errors in Table 4. The light curve fits have a median reduced chi-squared of 1.03, and

the residuals are Gaussian according to a Shapiro-Wilk test and within 10% of the predicted photon noise limit.

3. DISCUSSION AND CONCLUSIONS

We used the the WFC3 instrument on the *Hubble Space Telescope* to observe transits of the super-Earth HD 97658b at wavelengths between $1.1 - 1.7$ μm. Our white-light transit fits produce consistent estimates of the transit times and planet star radius ratios between the two visits. Our errors for these parameters are dominated by systematic noise, as illustrated in Fig. $1 - 3$. We combine our measured transit times with previously published values from *MOST* and *Spitzer* and show that they are consistent with a linear ephemeris. We also derive an improved estimate for the planet's orbital period with an uncertainty that is a factor of thirty smaller than in Van Grootel et al. (2014). Our average radius ratio is 2.5σ larger than the *Spitzer* 4.5 μm measurement from Van Grootel et al. (2014), and is in good agreement with the *MOST* visible-light value from Dragomir et al. (2013). It is unlikely that this offset is due to stellar activity as this star has a $\log(R'_{HK})$ value between -4.95 and -5.00 (Howard et al. 2011) and varied by less than 0.2% in brightness over a single 1.5 day visible-light observation by *MOST* (Dragomir et al. 2013).

We obtain nearly identical versions of the transmission spectrum (median difference of 0.75σ in individual bins) using the spectral template fitting technique (Deming et al. 2013; Knutson et al. 2014) and the white light residual method (Kreidberg et al. 2014), as shown in Fig. 7. Our median uncertainties on the differential wavelength-dependent transit depth are 19 ppm from both methods, making these observations the most precise measurement of a planetary transmission spectrum that we are aware of with WFC3 to date. Both versions of our spectrum display a slight upward slope towards redder wavelengths, and small modulations in flux around 1.30 and 1.45 μm. Neither feature is detected at a statistically significant level, and we therefore do not consider them in our subsequent comparison to atmosphere models for this planet.

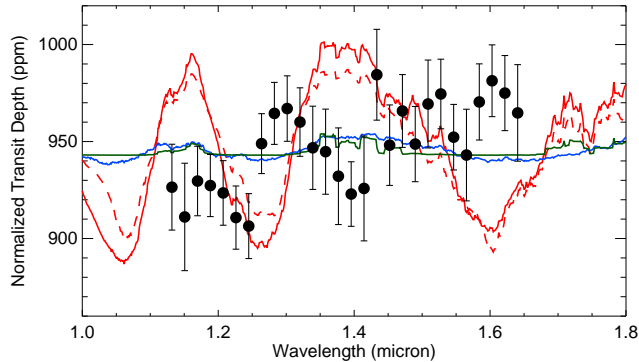In Fig. 8 we compare our measured transmission spec-

FIG. 8.— Wavelength-dependent transit depths averaged over the two visits (black filled circles). Four different atmosphere models are shown for comparison: a solar metallicity model (red solid line), a 50× solar metallicity model (red dashed line), a pure water model (solid blue line), and a solar metallicity model with an opaque cloud deck at 1 mbar (solid green line). The average depth for each model has been normalized to match the average measured transit depth in this plot.

trum from the spectral template fitting technique to several representative atmosphere models for HD 97658b, which are calculated following Kempton et al. (2012). The effective temperatures $(720 - 730$ K, depending on the model) and corresponding pressure-temperature profiles of these models are calculated assuming full redistribution of energy to the planet's night side and an albedo which varies according to composition. We consider both cloud-free models with solar and 50× solar metallicities, as well as a pure water model and a solar metallicity model with a high cloud deck located at one mbar. We calculate the significance with which our data can rule out a given model using the equation from Gregory (2005):

$$Significance = \frac{\chi^2 - \nu}{\sqrt{2\nu}} \qquad (3)$$

where χ^2 is calculated by comparing our averaged transmission spectrum to each model and ν is the number of degrees of freedom in the fit (27 in our case, as there are 28 points and we normalize the models to match the average measured transit depth of our data). This metric assumes that our measurement errors are Gaussian and uncorrelated from one wavelength bin to the next; although this is almost certainly untrue at some level, it represents a reasonable starting point for comparing different models. Following this approach we find that our measured transmission spectrum is inconsistent with the solar and 50× solar cloud-free models at the 17σ and 14σ levels, respectively. It is equally well described by the water-dominated (2.0σ) model and the solar metallicity model with optically thick clouds at a pressure of one mbar (1.9σ), as well as a flat line at the average transit depth across the band (1.6σ). We find that a solar metallicity model with clouds at 10 mbar is modestly inconsistent with the data (3.8σ), indicating that the clouds must be located at pressures below 10 mbar in this scenario. We note that there are any number of high metallicity atmosphere models that could provide a fit comparable to that of the pure water model; all our data

appear to require is either a relatively metal-rich atmosphere with a correspondingly small scale height, or the presence of a high cloud deck that obscures the expected water absorption feature in a hydrogen-dominated atmosphere. We constrain the maximum hydrogen content of the atmosphere in the first scenario by considering a series of cloud-free models with varying number fractions of molecular hydrogen and water, and find that in this scenario the atmosphere has to be at least 40% water by number in order to be consistent with our data at the 3σ level.

The conclusion that HD 97658b's transmission spectrum appears to be flat at the precision of our data places it in the same category as both the super-Earth GJ 1214b (Kreidberg et al. 2014) and the Neptune-mass GJ 436b (Knutson et al. 2014). As with these two planets, a more precise measurement of HD 97658b's transmission spectrum will eventually allow us to distinguish between high clouds and a cloud-free, metal-rich atmosphere. Our constraints on the atmospheric scale height in the cloud-free scenario are relatively weak compared to those obtained for GJ 1214b and GJ 436b, despite the fact that we achieve smaller errors (20 ppm vs 30 ppm) in our measurement of the differential transmission spectrum. This is primarily because HD 97658b has a smaller planet star radius ratio than either of these systems, and the predicted amplitude of the transmission spectrum is correspondingly small. Fortunately, it also orbits a brighter star than either GJ 1214b or GJ 436b, making it possible to achieve high precision transit measurements with relatively few observations. Unfortunately, this makes ground-based observations particularly challenging as the nearest comparison star with a comparable brightness is located more than $40'$ away. For space telescopes such as *Hubble* and *Spitzer*, achieving the precision required to study this planet in detail will mean pushing the systematic noise floor to unprecedentedly low levels. There is every reason to believe that this level of performance should be achievable, and given the unique nature of this planet it is likely that this will be put to the test in the near future.

REFERENCES

Allard, F., Homeier, D., & Freytag, B. 2012, Phys Trans of Royal Soc A, 370, 2765

Batalha, N. M. et al. 2013, ApJS, 204, 24

Bean, J. L., Miller-Ricci Kempton, E., & Homeier, D. 2010, Nature, 468, 669

Bean, J. L. et al. 2011, ApJ, 743, 92

Benneke, B. & Seager, S. 2012, ApJ, 753, 100

Benneke, B. & Seager, S. 2012, ApJ, 778, 153

Berta, Z. K. et al. 2012, ApJ, 747, 35

Burke, C. J. et al. 2014, ApJS, 210, 19

Carter, J. A. & Winn, J. N. 2009, ApJ, 704, 51

Charbonneau, D. et al. 2009, Nature, 462, 891

Chiang, E. & Laughlin, G. 2013, MNRAS, 431, 3444

Claret, A. 2000, A&A, 363, 1081

Demory, B.-O. et al. 2011, A&A, 533, A114

Deming, D. et al. 2013, ApJ, 774, 95

Désert, J.-M. et al. 2011, ApJ, 731, L40

Dragomir, D. et al. 2013, ApJ, 772, L2

Eastman, J., Siverd, R., & Gaudi, B. S. 2010, PASP, 122, 935

Fabrycky, D. C. et al. 2012, ApJsubmitted, arXiv:1202.6328

Fortney, J. J. et al. 2013, ApJ, 775, 80

Fressin, F. et al. 2013, ApJ, 766, 81

Gregory, P. Bayesian Logical Data Analysis for the Physical Sciences 167 (Cambridge Univ. Press, 2005).

Hadden, S. & Lithwick, Y. 2013, ApJsubmitted, arXiv:1310.7942

Hansen, B. M. S. & Murray, N. 2012, ApJ, 751, 158

Heng, K. & Kopparla, P. 2012, ApJ, 754, 60

Howard, A. W. et al. 2011, ApJ, 730, 10

Howard, A. W. et al. 2012, ApJS, 201, 15

Hu, R. & Seager, S. 2014, ApJsubmitted, arXiv:1401.0948

Kempton, E. M.-R., Zahnle, K., & Fortney, J. J. 2012, ApJ, 745, 3

Knutson, H. A. et al. 2014, Nature, 505, 66

Kreidberg, L. et al. 2014, Nature, 505, 69

Lissauer, J. J. et al. 2011, ApJS, 197, 8

Lithwick, Y., Xie, J., & Wu, Y. 2012, ApJ, 761, 122

Lopez, E. D., Fortney, J. J., & Miller, N. 2012, ApJ, 761, 59

Lopez, E. D. & Fortney, J. J. 2013, ApJ, 776, 2

Mandel, K. & Agol, E. 2002, ApJ, 580, L171

Mandell, A. M. et al. 2013, ApJ, 779, 128

Marcy, G. W. et al. 2014, ApJS, 210, 20

McCullough, P. R. & MacKenty, J. 2012, Instrument Science Report WFC3 2012-08 (Baltimore: Space Telescope Science Institute)

McCullough, P. R. et al. 2014, ApJsubmitted

Miller-Ricci, E., Seager, S., & Sasselov, D. 2008, ApJ, 690, 1056

Morley, C. V. et al. 2013, ApJ, 775, 33

Mortier, A. et al. 2013, A&A, 558, A106

Nettelmann, N., Fortney, J. J., Kramm, U., & Redmer, R. 2011, ApJ, 733, 2

Petigura, E. A., Marcy, G. W., & Howard, A. W. 2013, Proc. Nat. Acad. of Sciences, 110, 19273

Raymond, S. N., Barnes, R., & Mandell, A. M. 2008, MNRAS, 384, 663

Raymond, S. N. & Cossou, C. 2014, MNRASin press, arXiv:1401.3743

Rogers, L. A. & Seager, S. 2010a, ApJ, 712, 974

Rogers, L. A. & Seager, S. 2010b, ApJ, 716, 1208

Rogers, L. A., Bodenheimer, P., Lissauer, J. J. & Seager, S. 2010, ApJ, 738, 59

Seager, S., Kuchner, M., Hier-Majumder, C. A., & Militzer, B. 2007, apj, 669, 1279

Steffen, J. H. et al. 2013, MNRAS, 428, 1077

Valencia, D., Sasselov, D. D., & O'Connell, R. J. 2007, ApJ, 665, 1413

Valencia, D., Guillot, T., Parmentier, V., & Freedman, R. S. 2013, ApJ, 775, 10

Van Grootel, V. et al. 2014, ApJin press, arXiv:1402.5850

Wakeford, H. R. et al. 2013, MNRAS, 435, 3481

Wilkins, A. N. et al. 2014, ApJin press, arXiv:1401.4464

Weiss, L. M. & Marcy, G. W. 2014, ApJ, 783, L6

Winn, J. N. et al. 2011, ApJ, 737, L18

Zeng, L. & Sasselov, D. 2013, PASP, 125, 227